Atmospheric
Measurement
Techniques

*Supplement of*

# Impact of particle size, refractive index, and shape on the determination of the particle scattering coefficient – an optical closure study evaluating different nephelometer angular truncation and illumination corrections

**Marilena Teri et al.**

*Correspondence to:* Bernadett Weinzierl (bernadett.weinzierl@univie.ac.at)

## S1 Data evaluation

In the following sections, details on the data evaluation of the laboratory experiment are reported. An overview of the data evaluation is given in Sec.4.2 and in Fig.2. of the main text.

### S1.1 Particle scattering coefficient

5 The Aurora 4000 polar nephelometer measured the particle scattering coefficient $\sigma_{sp,\lambda}^{Aurora4000,\alpha}$ for 18 positions of the shutter: for $\alpha = 0°$ and for $\alpha$ in the range $10 - 90°$ with $5°$ resolution at three different wavelengths: blue ($\lambda_B = 450\,\mathrm{nm}$), green ($\lambda_G = 525\,\mathrm{nm}$), and red ($\lambda_R = 635\,\mathrm{nm}$). This setting led to a temporal resolution of $26 - 36\,\mathrm{s}$. The calibration was performed with particle-free air and $CO_2$. In addition, several calibration checks were performed before, during, and after the experiment period, as recommended by Anderson and Ogren (1998). All data from the Aurora 4000 polar nephelometer were corrected

10 using the average of all calibration checks performed (e.g., for $\alpha = 0°$ and $\lambda_G = 525\,\mathrm{nm}$, slope $= 1.003 \pm 0.008$, offset $= -0.4 \pm 0.2\,\mathrm{Mm^{-1}}$ ) and converted to standard temperature and pressure (STP $T_0 = 273.15\,\mathrm{K}$ $P_0 = 1013.25\,\mathrm{hPa}$). The error (90 % of confidence) of the total scattering coefficient due to calibration is within $\pm 3\,\%$, in agreement with the uncertainty of 2.5 % given in the Aurora 4000 user manual. The Rayleigh scattering coefficients at STP were subtracted, and the Aurora 4000 particle scattering coefficients ($\sigma_{sp,\lambda}^{Aurora4000,\alpha}$), not corrected for angular truncation and illumination error, were obtained. The

15 combined uncertainty due to calibration and noise for 1 minute data was within $\pm 8\,\%$, while for the average data along the selected sequences it was within $\pm 3\,\%$.

### S1.2 Particle phase function

The Horvath's polar nephelometer, a self-built polar nephelometer by Horvath et al. (2018), measured the angular distribution of the light scattered by particles without angular integration, i.e., the particle phase function ($P(\theta)$ at $\lambda = 532\,\mathrm{nm}$). Its detector

20 was mounted on a rotating arm with an angular resolution of $5°$, which was moved between 5 and $175°$ detecting the light scattered into its direction. A complete measurement cycle took $35\,\mathrm{min}$. Calibrations were performed with $CO_2$ and particle-free air very frequently, every measurement day twice a day, to check the stability of the light source. The Rayleigh scattering coefficient values of the calibration gases are considered at standard temperature and pressure (STP $T_0 = 273.15\,\mathrm{K}$ $P_0 = 1013.25\,\mathrm{hPa}$). The phase function was obtained by dividing the measured signal at every angle by the integral of all angles.

25 The Rayleigh scattering coefficient at STP was subtracted so that the phase function is for particles only. The extrapolation procedure described in (Horvath, 2015) was used to extend the particle phase function to $\theta = 0°$ and $\theta = 180°$. The accuracy of the full integration of the particle phase function given by this procedure is $1\,\%$. Since one measurement cycle took $35\,\mathrm{min}$, the shape of the measured particle phase function may be affected by changes in the aerosol concentration. During dust measurements, the aerosol concentration was very variable. Thus, the measured particle phase function was corrected using

30 the $1-$minute average signal from the Aurora 4000 polar nephelometer. The Horvath's polar nephelometer signal subtracted by the Rayleigh scattering is divided by the Aurora 4000 particle scattering coefficient at $0°$ at $\lambda_G = 525\,\mathrm{nm}$, $\sigma_{sp,\lambda_G}^{Aurora4000,0°}$. Since $\sigma_{sp,\lambda_G}^{Aurora4000,0°}$ is proportional to the light scattered by particles, the value obtained at each angle is proportional to the particle angular scattering function $\gamma_p(\theta)$. The particle phase function $P_p(\theta)$ is obtained by normalization.

For the data collected during this experiment, there are few cases were the extrapolation procedure performed to extend the

35 particle phase function to $\theta = 0°$ leads to a decreasing particle phase function from $\theta = 10°$ to $\theta = 0°$. These results were considered unrealistic and these measurements were excluded in further data analysis.

### S1.3 Particle extinction coefficient

The particle extinction coefficient $\sigma_{ep}$ at $\lambda = 530\,\mathrm{nm}$ was measured by a Cavity Attenuated Phase Shift Spectroscopy extinction Monitor(CAPS PM$_{ext}$ Monitor, Aerodyne). The CAPS PM$_{ext}$ performed automatically a zero measurement every 5

40 minutes. The given particle extinction coefficient $\sigma_{ep}$ was converted to standard temperature and pressure (STP $T_0 = 273.15\,\mathrm{K}$ $P_0 = 1013.25\,\mathrm{hPa}$). The instrument was calibrated by comparing the particle extinction coefficient $\sigma_{ep}$ measured for 203 nm PSL particles at low particle concentration ($< 100\,\mathrm{Mm^{-1}}$) with the particle scattering coefficient $\sigma_{sp}$, corrected for angular truncation and illumination error using the angular correction $C_{phase}$. For this purpose, the particle phase function was

simulated considering a log-normal size distribution with geometric median diameter $d_g = 203$ nm and geometric standard deviation $\sigma_g = 1.026$. The refractive index was $1.582 + i0.000$ for $\lambda = 525$ nm (Devon and Rudin, 1987). Between $15\%$ and $30\%$ of the particles were bi-spheres as indicated by the size spectra from the Ultra-High Sensitivity Aerosol Spectrometer (UHSAS, DMT). Scattering by the bi-sphere was simulated using a bisphere code (Mishchenko and Mackowski, 1994). The miepython module developed by Scott Prahl and based on Wiscombe (1980) was used for the single spheres. The angular correction obtained was $C_{phase} = 1.011 \pm 0.002$. During the experiment, the CAPS $PM_{ext}$ was accidentally evacuated. The evacuation may cause contamination of the mirrors, consequently an increase of the loss of signal, and thus a decrease of sensitivity. However, the loss of signal registered after the event is lower than the maximum value of $1000$ $Mm^{-1}$ recommended by the manufacturer. Therefore, measurement data after the event can still be used. All polydisperse aerosol measurements were performed before the event. Only a few PSL and ammonium sulfate monodisperse aerosol measurements were performed after the event. Two different calibrations are used: before the event slope $= 1.02 \pm 0.01$, after the event slope $= 1.22 \pm 0.02$. The calibration correction included a second degree term ($= 8 \cdot 10^{-5}$ Mm) to correct for non linear behavior of the CAPS $PM_{ext}$ at high particle extinction coefficient ($> 200$ $Mm^{-1}$). This term was obtained during a previous intercomparison experiment at the TROPOS institute by comparing the particle extinction coefficient measured with the particle scattering coefficient for 200 nm PSL particles in the range $0 - 2000$ $Mm^{-1}$. The accuracy of the particle extinction coefficient measured by the CAPS $PM_{ext}$ was $\pm 3\%$ according to Petzold et al. (2013) and Onasch et al. (2015).

## S1.4 Particle absorption coefficient

The particle absorption coefficient $\sigma_{ap}$ at wavelengths $467$ nm, $528$ nm, $652$ nm was measured by a tri-color absorption photometer (TAP, Brechtel). We used $47$ mm diameter glass-fiber Pallflex E70-2075W filters that are well characterized and have been used widely also with other absorption photometers such as the Particle Soot Absorption Photometer (PSAP, Radiance Research) (Bond et al., 1999; Müller et al., 2014; Virkkula, 2010; Virkkula et al., 2005; Ogren et al., 2017; Davies et al., 2019). The white filter check was performed following the manufacturer indications. The diameter of each of the 10 spots was measured with a caliber for three times. Average value of all measurements is $d = 7.5 \pm 0.2$ mm, with coefficient of variation $2\%$, yielding to a spot area of $43.9 \pm 2.3$ $mm^2$. The TAP sample flow was controlled downstream of the measurement cell by a mass flow meter (MFM, Alicat scientific) and measured by an internal flow meter. The sample flow was calibrated with a bubble flow meter (Gilibrator 2, Gilian) at different pressures. The obtained linear least square regression parameters (slope $= 0.961 \pm 0.004$, offset $= -0.06 \pm 0.01$ Std L min$^{-1}$, $R^2 = 0.99997$) are used to correct the measured sample flow. The calculated actual volume flow rate was $1.99 \pm 0.02$ L min$^{-1}$. Data were converted to standard temperature and pressure (STP $T_0 = 273.15$ K $P_0 = 1013.25$ hPa). The 1-minute average absorption coefficients are corrected using the correction scheme developed by Bond et al. (1999); Ogren (2010), using the 1-minute average Aurora 4000 scattering coefficient non-corrected for angular truncation and illumination error. The filter transmission during all measurements was larger than $0.90$, higher than the lower limit ($= 0.7$) of the Bond et al. (1999) correction scheme. The single scattering albedo SSA, calculated on the basis of particle extinction coefficient measured by the CAPS $PM_{ext}$ at $\lambda = 530$ nm and absorption measured by the TAP at $\lambda = 528$ nm, for mineral dust measurements is in the range $0.95 - 0.99$, in agreement with literature values (Ansmann et al., 2011; Schladitz et al., 2009; Müller et al., 2011b; Petzold et al., 2011). Ogren et al. (2017) estimated the uncertainty associated with the Bond et al. (1999) algorithm as function of the SSA and the raw absorption coefficient for 30 min averaging absorption coefficient. The raw absorption coefficient $> 3$ $Mm^{-1}$ and the single scattering albedo SSA$= 0.95 - 0.99$, during mineral dust measurements, lead to an uncertainty of the absorption coefficient increasing with SSA from $35\%$ to $100\%$. Since we used weakly absorbing aerosol only, the high relative uncertainty of the particle absorption coefficient has only a very limited effect on the uncertainty of the difference between the particle extinction coefficient and the particle absorption coefficient, i.e., the value considered as a reference in this work.

## S1.5 Particle size distribution

The particle size distribution was measured with an Ultra-High Sensitivity Aerosol Spectrometer (UHSAS, DMT) in the range $60 - 1000$ nm and by an Optical Particle Sizer (OPS 3330, TSI) in the range $0.3 - 10$ µm. Moreover, the total particle number concentration in the size range from $10$ nm to $> 3$ µm was measured by a condensation particle counter (CPC 3772, TSI).

For each instrument, the particle number concentration was calculated from the 1-second count rate and the aerosol flow. The flows were calibrated using a bubble flow meter (Gilian 2, Gilibrator), leading to a volume flow of $53.3 \pm 0.2 \, \mathrm{cm^3 \, min^{-1}}$ for the UHSAS, $1.00 \pm 0.05 \, \mathrm{L \, min^{-1}}$ for the OPS, $1.06 \pm 0.01 \, \mathrm{L \, min^{-1}}$ for the CPC. Concentrations were corrected to standard temperature and pressure (STP $T_0 = 273.15 \, \mathrm{K}$ $P_0 = 1013.25 \, \mathrm{hPa}$) and 1 min average data were produced to reduce noise.

The OPS and UHSAS counting efficiency was estimated comparing their total particle number concentration with the CPC particle number concentration for measurements of monodisperse ammonium sulfate aerosol, where the size was selected with the DMA. Nominal sizes chosen were $402, 501, 602, 702, 850 \, \mathrm{nm}$ for the comparison with the OPS and $200, 301, 402, 501, 602, 702 \, \mathrm{nm}$ for the one with the UHSAS. The maximum particle number concentration measured by the CPC was $250 \pm 25 \, \mathrm{cm^{-3}}$ for the comparison with the OPS and $1330 \pm 130 \, \mathrm{cm^{-3}}$ for the comparison with the UHSAS, well below the single-particle counting limit of $10^4 \, \mathrm{cm^{-3}}$ reported by the CPC user manual. The error reported for the CPC particle number concentration is the accuracy of $\pm 10 \, \%$ given by the manufacturer. The least-square linear regression forced through the origin led to a slope of $1.059 \pm 0.005$ ($R^2 = 0.9999$) for the OPS and of $0.901 \pm 0.004$ ($R^2 = 0.9999$) for the UHSAS. The high $R^2$ indicates that coincidences were not occurring for UHSAS and OPS in the considered particle number concentration range.

For this comparison, the OPS and UHSAS particle number concentration of each size bin was corrected for particle loss considering the CPC and OPS or UHSAS particle transmission of the corresponding volume-equivalent diameter (for particle loss calculation see Sec.S1.6). The correction factor for the UHSAS to the CPC transmission varies with size in the range $1.02 - 1.09$. The total UHSAS efficiency increased by $3 \, \%$ after the correction was applied. The correction factor for the OPS to the CPC increases monotonically with particle size from 1.00 to 1.07. However, the correction factor is lower than 1.01 up to $3.5 \, \mathrm{\mu m}$. Considering the particle loss correction, the OPS efficiency decreased by $0.1 \, \%$.

For all the measurements performed during the experiment, the OPS total particle number concentration was below the single-particle counting limit of $1000 \, \mathrm{cm^{-3}}$ reported by the OPS user manual and the dead time correction was unnecessary. The UHSAS total particle number concentration exceeds the single-particle counting limit of $3600 \, \mathrm{cm^{-3}}$ in four cases only, i.e., for PSL particles with nominal diameter $0.097, 0.9, 1.6, 1.8 \, \mathrm{\mu m}$. In these cases the UHSAS measures a large amount of very small residual particles that are formed from the PSL liquid when it is evaporated. Since those small particles have a very small contribution to the particle scattering coefficient, no correction was applied.

The calibration of UHSAS and OPS was performed with PSL particles before the experiment. The accuracy of the calibration was checked using the PSL particle measurements performed during the experiment. A log-normal fit was performed for each particle size distribution and the geometric mean diameter obtained was compared with the nominal diameter. Least-square linear regression led to a slope of $0.96 \pm 0.01$ and an offset of $18 \pm 10 \, \mathrm{nm}$ ($R^2 = 0.999$) for the OPS calibration, in agreement with the particle sizing uncertainty of $\pm 5 \, \%$ given by the manufacturer; a slope of $1.001 \pm 0.004$ and an offset of $0.4 \pm 1.4 \, \mathrm{nm}$ ($R^2 = 0.9999$) for the UHSAS calibration when using the linear map for the size binning of the UHSAS; a slope of $0.999 \pm 0.002$ and an offset of $0.9 \pm 1 \, \mathrm{nm}$ ($R^2 = 0.9999$) for the UHSAS calibration when using the logarithmic map, within the particle sizing uncertainty of $\pm 2.5 \, \%$ given by the manufacturer.

Comparison between the particle number concentration in overlapping bins ($374 - 721 \, \mathrm{nm}$) led to an agreement within $1 - 5 \, \%$ for PSL particles measurements (nominal diameter $= 400, 508, 565, 600, 700 \, \mathrm{nm}$), within $2 - 15 \, \%$ for AS measurements (nominal diameter $= 400, 508, 565, 600, 700 \, \mathrm{nm}$), within $5 - 20 \, \%$ for mineral dust measurements. PSL equivalent size distributions were obtained for all aerosol samples by combining the UHSAS particle size distribution in the range $0.06 - 0.374 \, \mathrm{\mu m}$ with the OPS particle size distribution in the range $0.374 - 10 \, \mathrm{\mu m}$.

## S1.6   Particle loss corrections

The particle loss in the tubes from the chamber to the different instruments was calculated with the Particle Loss Calculator software (PLC, von der Weiden et al. (2009)). Settings for the calculations were ambient temperature $T = 20 \, \mathrm{C}$ and ambient pressure $P = 1013 \, \mathrm{hPa}$. The aerosol density $\rho_0 = 1 \, \mathrm{g \, cm^{-3}}$ and shape factor $\chi_0 = 1$ were chosen to get the particle transmission as function of the aerodynamic equivalent diameter ($d_{ae}$). The particle transmission along the tubing system of all instruments was in the same range except for the UHSAS and the OPS. In particular, the maximum and minimum transmission ($T_{max}$ and $T_{min}$) among the transmissions of all optical properties instruments (Aurora 4000, Horvath's polar nephelometer, CAPS PM$_{ext}$ and TAP) differ with their midpoint transmission (($T_{min} + T_{max})/2$) by less than $\pm 0.01$ for $d_{ae} = 0.06 - 1.00 \, \mathrm{\mu m}$ and less than $\pm 0.07$ for $d_{ae} = 1.00 - 10.00 \, \mathrm{\mu m}$. Considering the midpoint transmission and the transmission of the OPS and

the UHSAS, the particle loss correction factor was calculated as function of the particle diameter $d_i$ as ($T_i^{mid}/T_i^{UHSAS}$, $T_i^{mid}/T_i^{OPS}$). The uncertainty of each correction factor is estimated considering the maximum and minimum transmission of optical properties instruments.

The aerodynamic equivalent diameter was converted to the volume-equivalent diameter $d_{ve}$ of each aerosol type considering their density $\rho_p$ and shape factor $\chi$ (PSL $\rho_p = 1.05$ gcm$^{-3}$, $\chi = 1$; AS $\rho_p = 1.77$ gcm$^{-3}$, $\chi = 1$; mineral dust $\rho_p = 2.6$ gcm$^{-3}$, $\chi = 1.25$):

$$d_{ve} = d_{ae} \left( \frac{\rho_p}{\rho_0 \chi} \right)^{-1/2} \tag{1}$$

Moreover, an additional correction is considered for the large sizes of mineral dust to take into account the effect of the non spherical shape on the sizing by the OPS. The optical form factor, the ratio between the extinction coefficient of a particle and the extinction coefficient of a volume-equivalent sphere is proportional to $\chi^2$ for size parameter larger than 10 ($d > 2.1$ μm for $\lambda_{OPS} = 660$ nm) (Pfeifer, 2014). We assume that the scattering cross section seen by the OPS is proportional to the particle extinction coefficient. Since for large size the particle extinction coefficient is proportional to the geometric cross section, the OPS diameter can be written:

$$d_{OPS} = d_{ve} \chi \tag{2}$$

Considering all aerosol types, the correction factor for the UHSAS varies within its detection size range ($0.06 - 1$ μm) from $1.021 \pm 0.002$ to $1.119 \pm 0.006$. The correction factor for OPS in the size range $0.3 - 1$ μm is negligible $1.000 \pm 0.001 - 0.998 \pm 0.005$; for the size range $1 - 3$ μm it is within $0.999 \pm 0.003 - 0.98 \pm 0.04$, still a small variation but with a larger error; for larger size (until 10 μm) the correction factor decreases until to $0.6 \pm 0.2$ for PSL particles, $0.4 \pm 0.3$ for AS and $0.5 \pm 0.2$ for mineral dust.

The particle number concentration of each size bin of OPS and UHSAS was corrected using the correction factor corresponding to the mid diameter of each bin was used. Simulations considering the maximum and minimum transmission yields to total particle scattering coefficient within $\pm 2.4$ % of the one obtained considering the midpoint transmission.

## S1.7 Sequence selection and temporal averaging

All data were recorded with 1-second resolution, except for the UHSAS which was set to accumulate counts for 10 s, the Aurora 4000 polar nephelometer which has $\sim 30$ s resolution for the measurement of $\sigma_{sp,\lambda}^{Aurora4000,0°}$, and the Horvath's polar nephelometer which takes 35 minutes to complete a cycle backward and forward from scattering angle $5°$ to $175°$. 1-minute averaging was performed for all data in order to reduce the noise, except for the Horvath's polar nephelometer. The time series for all data was visually compared with the time series of the CPC particle number concentration to check the time synchronization. Moreover, the 1-minute average data were used for corrections where data from more instruments were required. For each measurement, sequences with constant particle number concentration and no change in the scattering Ångström exponent SAE($\lambda_G$, $\lambda_R$) were selected and all data were averaged along with the sequences. If a measurement with the Horvath's polar nephelometer was available, the data were averaged along the corresponding 35 minutes. Even if the particle number concentration is not constant, the result is not affected as long as the average is performed for the same time period for all instrumentation. No significant variation of the scattering Ångström exponent SAE($\lambda_G$, $\lambda_R$) were observed during the selected sequences.

## S1.8 Optical simulations using measured particle size distribution

The measured particle size distributions were used to simulate via scattering theory the optical properties of the measured aerosols. In particular, the particle scattering coefficient, the particle extinction coefficients, and the particle phase function were simulated for each selected sequence considering the PSL equivalent size distribution obtained merging the UHSAS($0.060 - 0.374$ μm) and OPS($0.374 - 10$ μm). The optical simulations were performed with the program MOPSMAP (Gasteiger and Wiegner, 2018), using the option to give the binned size data directly as input. We considered spherical shapes only (Mie

code) and as refractive index we used the refractive index of PSL particles. $m = 1.591 + i0.00$ was used for $\lambda = 450\,\mathrm{nm}$, $m = 1.582 + i0.00$ for $\lambda = 525\,\mathrm{nm}$, $m = 1.574 + i0.000$ for $\lambda = 635\,\mathrm{nm}$ (Devon and Rudin, 1987). This choice has been made to be consistent with the particle size distribution used as input where a PSL particle refractive index was used for the inversion. The simulated particle phase function was integrated considering the Aurora 4000 angular sensitivity function and the simulated Aurora 4000 scattering coefficients non corrected for angular truncation and illumination error were calculated. The uncertainty of the simulated values was estimated by repeating the simulations 1000 times with input binned size data randomly modified within their uncertainty. For modification of the particle number concentration a normal distribution with mean = 1 and standard deviation = 0.05 was assumed. This choice has been made considering the largest uncertainty over the particle number concentration of $\pm 10\,\%$ given by the CPC accuracy and introduced using the CPC to estimate the UHSAS and OPS efficiency. We assumed that the CPC manufacturer accuracy represents a 95 % confidence interval. For modification of the bin diameter a normal distribution with mean = 1 and standard deviation = 0.025 was assumed. This choice is consistent with the $\pm 2.5\,\%$ sizing uncertainty of UHSAS and $\pm 5\,\%$ sizing uncertainty of OPS reported by the manufacturers and confirmed by the calibration check with PSL particles. The 95 % confidence interval over simulated values was estimated considering the $2.5th$ and $97.5th$ percentiles.

## S2   Measured particle extinction coefficient vs simulated particle extinction coefficient

To test the consistency between the particle size distribution measurements and the optical measurements, we compared the simulated particle extinction coefficient with the particle extinction coefficient measured by the CAPS $PM_{ext}$. Fig.S1 shows the comparison for all selected sequences. The linear regression forced through the origin weighted considering the inverse of the variance of the simulation results leads to an excellent agreement for PSL particles and ammonium sulfate (AS) measurements with slope $= 0.94 \pm 0.02$ and coefficient of determination $R^2 = 0.987$, slightly lower than the 3 % accuracy of CAPS $PM_{ext}$.

For polydisperse measurement of mineral dust, silica and volcanic ash the weighted least squares forced through the origin leads to slope $= 1.05 \pm 0.03$ and $R^2 = 0.991$ for cases where the measured volume median diameter (VMD) was smaller than $2\,\mu\mathrm{m}$ and to slope $= 1.20 \pm 0.02$ and $R^2 = 0.995$ for cases with VMD $> 2\,\mu\mathrm{m}$.
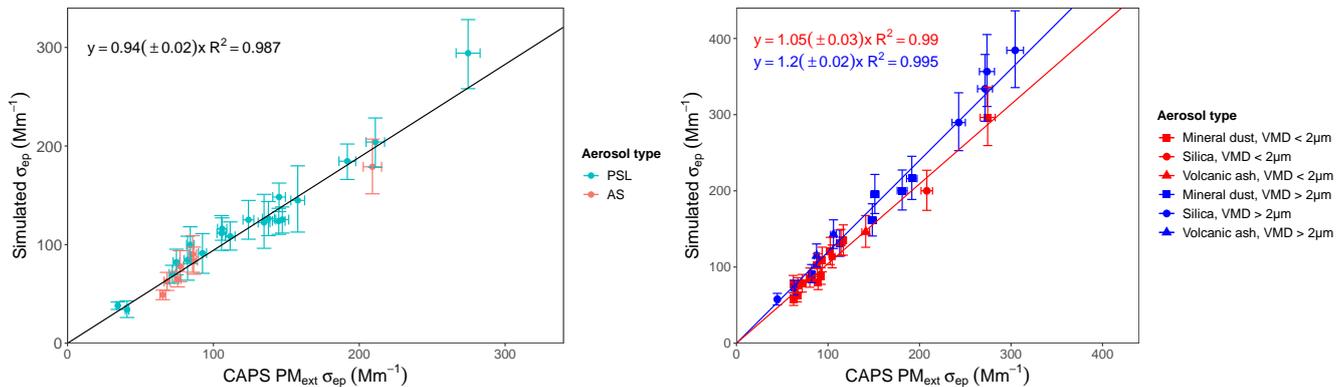


**Figure S1. Comparison of the simulated particle extinction coefficient with the particle extinction coefficient measured by CAPS $PM_{ext}$.** The left panel shows the result for PSL particles measurements (light blue) and ammonium sulfate (AS) measurements (orange). The right panel shows the result for mineral dust, silica and volcanic samples for volume median diameter smaller than $2\,\mu\mathrm{m}$ (red) and volume median diameter larger than $2\,\mu\mathrm{m}$ (blue). Reported error bars are the instrumental accuracy of 3 % for CAPS $PM_{ext}$ and $2.5th$ and $97.5th$ percentiles for the simulations.

In order to explain these discrepancies for the case with large dust we performed model calculations with the discrete dipole approximation code ADDA (Yurkin and Hoekstra, 2011) for dust particles considering three different irregular shapes (C, D,

and F from Gasteiger et al. (2011)), different refractive indices ($1.50 + i0.00$ and $1.55 + i0.00$), a volume-equivalent diameter range upto about $5\,\mu m$ and 18000 particle orientations.

Figure S2 shows in the left panel a flow chart of the calculations. The simulated OPS cross-sections ($\lambda = 660\,nm$) for the
205 irregular mineral dust are inverted assuming a smoothed Mie curve for PSL spheres with refractive index $1.572 + i0.000$. The inverted diameters are combined with PSL particles refractive index $1.582 + i0.000$ to simulate the particle extinction coefficient at the wavelength of the CAPS $PM_{ext}$ ($\lambda = 530\,nm$) which are then compared to the particle extinction coefficient of the irregularly shaped particle at this wavelength. The right panel of Fig.S2 shows the ratio between the particle extinction coefficient derived via the PSL-based OPS size inversion and the directly simulated particle extinction coefficient as function of
210 diameter. According to the simulations, it can be expected that the derived particle extinction coefficient by coarse particles is overestimated by $10 - 40\,\%$. This overestimation can explain the slope$= 1.2$ found for VMD $> 2\,\mu m$ from our measurements. On the other hand, the overestimation for coarse particles might be compensated by an underestimation for fine particles, if they contribute enough to the mineral dust aerosol as in case of VMD $< 1\,\mu m$.
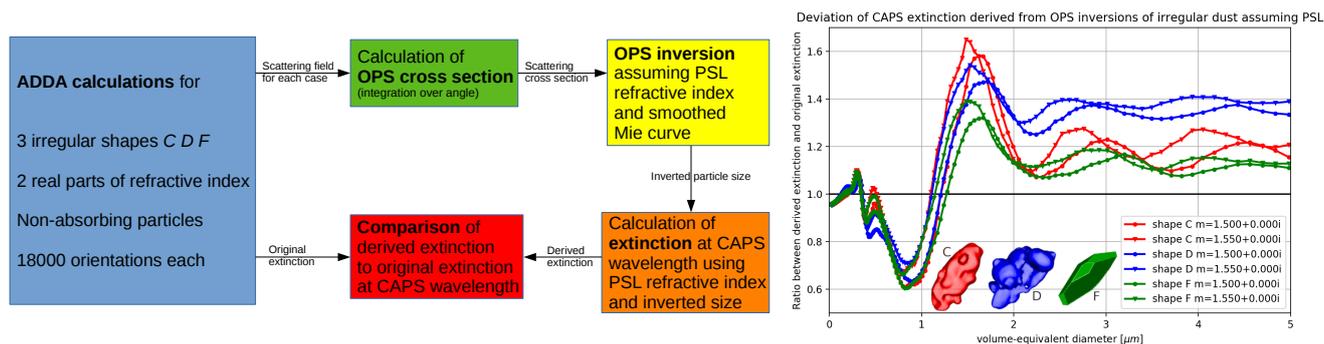


**Figure S2. Simulations of the particle extinction coefficient discrepancies for irregularly shaped dust particles when PSL spheres are assumed for OPS size inversion.** The left panel shows a flow chart of the simulations. The right panel illustrates the simulated ratio between the derived particle extinction coefficient and the original particle extinction coefficient of the irregularly shaped particle as function of the particle size at $\lambda = 530\,nm$ the CAPS $PM_{ext}$ wavelength. The colors illustrate results for three different irregular shapes with non-absorbing refractive indices $1.50 + i0.00$ and $1.55 + i0.00$.

## S3   Sensitivity of the TSI OPS 3330 to particle refractive index and shape

215 An optical particle sizer, such as the TSI OPS 3330, measures the particle scattering cross sections and sorts particles into different size bins based on their detected scattering cross section. For the TSI OPS 3330, the manufacturer provides nominal diameter values for the bin boundaries for the calibration material, i.e., PSL particles with refractive index m = 1.59 + i0.00 and spherical shape. The particle size distribution obtained with such a measurement is a PSL-equivalent size distribution. Any deviation from the refractive index or shape of the calibration material will increase the uncertainty of the derived particle size 220 distribution.

Figure S3 shows the relationship between the TSI OPS 3330 scattering cross section and the particle volume-equivalent diameter for the calibration material (in black) and for different refractive indices in the range of mineral dust particles, both in the case of spherical particles and in the case of irregularly shaped particles.
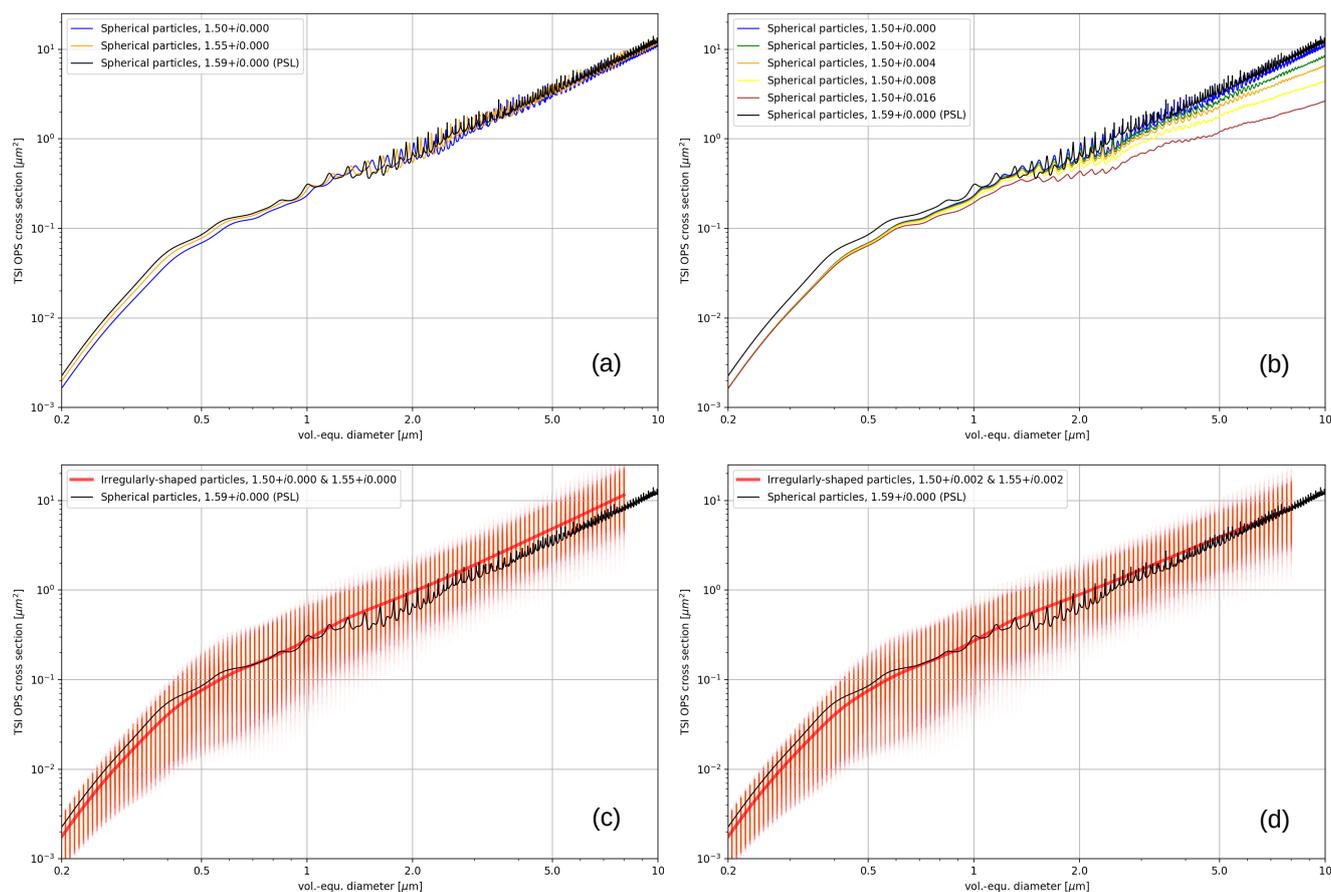


**Figure S3. Scattering cross section modeled for the TSI OPS 3330.** The black line in all four panels is the TSI OPS 3330 scattering cross section for PSL particles, i.e., the calibration material (m= 1.59 + i0.00 and spherical shape). In addition, each panel shows the TSI OPS 3330 scattering cross section for particles with different refractive indices or shapes relevant for mineral dust particles: (a) non-absorbing spherical particles with different real part of the refractive index (n= 1.50, 1.55); (b) spherical particles with different imaginary part of the refractive index (k = 0.000, 0.002, 0.004, 0.008, 0.016); (c) non-absorbing and (d) slightly absorbing irregularly shaped particles. Red dots correspond to 18000 orientations of six different mineral dust shapes (Gasteiger et al., 2011) and the red line is the average.

The TSI OPS 3330 scattering cross section of coarse-mode particles (d > 1 μm) is not very sensitive to the real part of the refractive index between m= 1.50 + i0.00 and m= 1.59 + i0.00 (Fig.S3a). Thus, the uncertainty of the PSL equivalent particle size distribution for non-absorbing spherical particles with mineral dust-like refractive index is negligible. The TSI OPS 3330 scattering cross section for coarse-mode particles is more sensitive to the imaginary part, and the PSL-equivalent diameters underestimate the diameter of absorbing particles (Fig.S3b). For example, a moderately absorbing spherical particle with imaginary part k= 0.004 and a diameter of about 5 μm would have the same scattering cross section as a PSL particle with about 4 μm diameter, and therefore, the OPS would size it with a PSL-equivalent diameter of about 4 μm.

If particles have an irregular shape, the relationship between TSI OPS 3330 scattering cross section and particle volume-equivalent diameter is more complex as also the shape and the orientation of the particle plays a role. Figure S3c and d show the TSI OPS 3330 scattering cross section for 6 irregular shapes typical for mineral dust (Gasteiger et al., 2011) in 18000 orientations (red dots). The average is indicated by the red line. Coarse non-absorbing irregular particles have, on average, a slightly increased scattering cross section with respect to spherical particles with the same volume-equivalent diameter (Fig.S3c). Therefore, the particle size is slightly overestimated by a TSI OPS 3330 calibrated with PSL particles. In case of slightly absorbing particles (e.g., with imaginary part ∼ 0.002) the TSI OPS 3330 calibrated with PSL has on average a better performance (Fig.S3d). Therefore, the effect of irregular shape might partly compensate the effect of the imaginary part of the refractive index.

Furthermore, the variability of the scattering cross section of irregularly shaped particles of fixed size might lead to additional effects on higher orders of the size, e.g., particle area or volume, so that the agreement of the average shown in Fig.S3d, does not necessarily result in good performance for higher orders using the same imaginary part. For any non linear function of the size separate investigations are needed.

## S4  Details of the simulated closure experiment

This section describes the details of the simulated closure experiment. Selected particle size distributions, refractive indices, and shapes are used as input to simulate the TSI OPS 3330 response. The angular correction $C_{phase,OPS}$ is obtained from the OPS particle size distributions through optical simulations considering different approaches, e.g., assuming different refractive indices or shapes. The angular correction $C_{phase,OPS}$ can be compared with the "original" $C_{0°}$, obtained simulating the Aurora 4000 polar nephelometer response for the corresponding particle size distributions, refractive indices, and shapes. The overview of the flow chart of the simulated closure experiment is given in Sec.5.1 and in Fig.4 of the main text.

We selected 5000 random samples with input particle size distributions and refractive indices similar to Anderson and Ogren (1998), Müller et al. (2011a) Bond et al. (2009) and Massoli et al. (2009). The particle size distributions were bimodal log-normal with geometric volume median diameter ranging from 0.2 to 0.4 μm for the fine mode and from 2.0 to 4.0 μm for the coarse-mode. The geometric standard deviations were selected for each mode in the range between 1.6 and 2.2. The fine mode volume fraction was varied between 0.1 and 0.9. For each case, either the complete particle size distribution (no size cut-off) or a particle size distribution with a nominal aerodynamic 1μm cut off (sub-micrometer size cut off) was considered. The sub-micrometer size cut off was modeled as a hyperbolic tangent function with a 50 % geometric diameter cut point at 0.85 μm and 10 % and 90 % transmission 0.05 μm above and below the cut point, similarly to Massoli et al. (2009). For homogeneous spherical particles, the refractive index was chosen among 1.33, 1.38, 1.4, 1.43, 1.48, 1.52, 1.53, 1.57, 1.59, 1.63, 1.70 for the real part and among 0.00, 0.001, 0.002, 0.005, 0.01, 0.03, 0.05, 0.10, 0.30 for the imaginary part.

Additionally, 1000 random samples were selected with refractive index similar to mineral dust particles: 1.5, or 1.55 for the real part and among 0.00, 0.002, 0.004, 0.008, 0.016 for the imaginary part. The calculations for these samples were repeated twice for homogeneous spherical particles and for irregular shapes selected among mineral dust shapes from Gasteiger et al. (2011).

Optical simulations for homogeneous spherical particles were performed with a Mie code (miepython module - https://github.com/scottprahl/miepython, developed by Scott Prahl and based on Wiscombe (1980)), and for irregularly shaped particles with the discrete dipole approximation (ADDA code - https://github.com/adda-team/adda, Yurkin and Hoekstra, 2011).

The original $C_{0\circ}$ was simulated for each selected refractive index, particle size distribution and shape considering the Aurora 4000 angular sensitivity function for $\alpha = 0°$. The selected refractive indices are referred hereafter as the true refractive index, $n_{true} + ik_{true}$.

The original angular correction $C_{0\circ}$ is referred hereafter as the spherical $C_{0\circ}$ or irregular $C_{0\circ}$ for homogeneous spherical particles or for irregularly shaped particles respectively. For the calculation of the irregular $C_{0\circ}$, we considered the average over the mineral dust-like irregular shapes (A-F) from Gasteiger et al. (2011), and 18000 particle orientations.

Calculations were performed on a diameter grid, selected with 1371 log-spaced diameters with resolution $dlog(d) \sim 0.00256$ in the size range, equivalent to the OPS diameter detection limits. The OPS diameter detection limits corresponding to each $n_{true} + ik_{true}$ were calculated via Mie theory considering the diameter detection limits of $0.3 - 10\,\mu m$ for homogeneous spherical particles with refractive index $1.59 + i0.00$ given by the manufacturer. For the irregularly shaped particle calculations, the diameter grid upper size was restricted to the upper size available for the ADDA calculations: $4.9\,\mu m$ for $\lambda_B = 450\,nm$, $5.8\,\mu m$ for $\lambda_G = 525\,nm$, $7.0\,\mu m$ for $\lambda_R = 635\,nm$.

The angular correction $C_{phase,OPS}$ corresponding to each original $C_{0\circ}$ was simulated with the following five steps (See steps 1-5 of the flow chart in Fig.4 of the main text):

**Step 1:** the signal measured by the TSI OPS 3330, the scattering cross section $C_{sca,i}$, was calculated for the selected true refractive index for each diameter of the grid $d_i$. In the case of homogeneous spherical particles, we calculated the OPS $C_{sca,i}$ using a (custom) Mie code based on Bohren and Huffman (2008), in which we considered the light polarization to calculate the intensity of the scattered light as a function of both scattering and azimuth angle. To obtain the OPS $C_{sca,i}$, we integrated the result over the spherical angle covered by the OPS detector. In case of irregular particles, we calculated the OPS $C_{sca,i}$ for each mineral dust-like shapes (A-F) from Gasteiger et al. (2011) using the ADDA code (Yurkin and Hoekstra, 2011). The orientations and shapes were selected randomly for each $d_i$. For different random samples, the results in terms of angular correction were affected less than $0.1\,\%$.

**Step 2:** the size selection executed by the TSI OPS 3330 was reproduced, i.e., each OPS $C_{sca,i}$ was assigned to a $bin_i$ from 1 to 16. The $C_{sca}$ values for the OPS bin boundaries were calculated from the PSL-equivalent nominal diameter bin boundaries provided by the manufacturer and the OPS Mie curve (i.e., the OPS $C_{sca}$ as a function of diameter) for the refractive index of $1.59 + i0.00$, i.e., the refractive index of PSL particles.

**Step 3:** the selected size distribution $dn/dlog(d)$ was considered by calculating the counts for each $bin_{j=1,16}$ as

$$Counts_{j=1,16} = \sum_{bin_i=j} \frac{dn_i}{dlog(d_i)} dlog(d_i), \tag{3}$$

The introduction of the selected particle size distribution at this step helps to reduce the computational time.

**Step 4:** the diameter values of the bin boundaries were selected with different approaches to obtain the binned size data. Either the nominal diameter values provided by the manufacturer for the PSL particle refractive index $(1.59 + i0.00)$ are used, or an inversion procedure is applied to obtain the bin boundaries for other refractive indices. In the latter case, we calculated the bin boundaries through a Mie curve inversion, considering a smoothed Mie curve of the true refractive index.

**Step 5:** the optical calculations to obtain the angular correction $C_{phase,OPS}$ were performed with the program MOPSMAP (Gasteiger and Wiegner, 2018). We used the MOPSMAP option to give the binned size data directly as input. Different approaches were applied to select the input refractive indices for the optical simulations.

Different approaches to run steps 4 and 5 are possible. We considered the following three possibilities:

**Approach a:** In step 4, the PSL-equivalent nominal diameter values for the OPS bin boundaries provided by the manufacturer were used to obtain the binned size data. In step 5, the angular correction $C_{phase,OPS}(a)$ for the randomly selected aerosol was calculated with Mie calculations. Input for the optical calculations were the binned size data obtained in step 4, the refractive index of PSL particles $(1.59 + i0.00)$ and the green wavelength of the Aurora 4000 nephelometer $(\lambda_G = 525\,nm)$.

**Approach b:** In step 4, the PSL-equivalent nominal diameter values for the OPS bin boundaries provided by the manufacturer were used to obtain the binned size data. In step 5, the angular correction $C_{phase,OPS}(b)$ was calculated for the randomly selected aerosol with Mie calculations assuming the true refractive index, i.e., the refractive index selected for corresponding random selected aerosol.

315 **Approach c:** In step 4, the diameter values of the bin boundaries were calculated by an inversion procedure assuming the true refractive index, i.e., the refractive index selected for each randomly selected aerosol. In step 5, the angular correction $C_{phase,OPS}(c)$ was calculated for the randomly selected aerosol with Mie calculations assuming the true refractive index.

None of the approaches considers the non-sphericity of the irregularly shaped particles in steps 4 or 5.

## S5 Relevance of particles in the size range $0.06 - 0.3 \,\mu m$

320 In order to calculate the angular correction, the particle size distribution in the diameter range $0.06 - 0.3 \,\mu m$ is relevant as well. We compared the original angular correction $C_{0°}$ calculated for the size range $0.06 - 10 \,\mu m$ and the TSI OPS 3330 diameter detection limits (Fig.S4). This comparison shows that considering only the OPS size range leads to an overestimation of the angular truncation and illumination error by $1\,\%$ up to $50\,\%$ for the calculations without size cut off and up to $10\,\%$ for the calculations with sub-micrometer size cut off, increasing with the imaginary part of the refractive index.
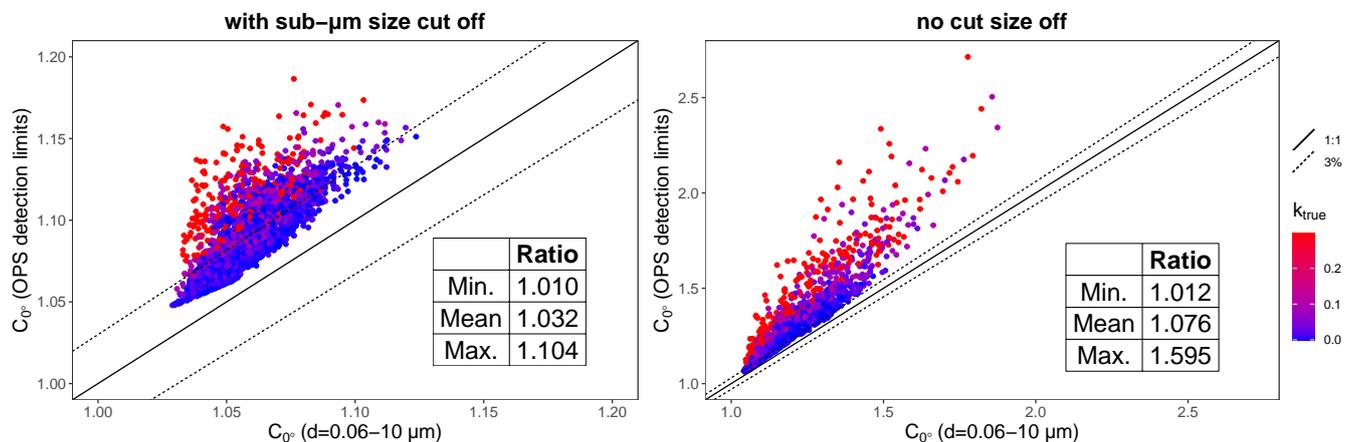


**Figure S4. Comparison between the angular correction calculated considering the size range** $0.06 - 10 \,\mu m$ **and considering the OPS detection limits.** Calculations are for the green wavelength ($\lambda = 525$ nm). The left panel shows the comparison for size distributions without a cut off. The right panel shows the comparison for size distributions with a sub-micrometer cut off applied. Different colors refers to different values of the imaginary part of the refractive index. The solid line is the $1:1$ line. The dashed lines are the $\pm 3\%$ lines.

# References

Anderson, T. L. and Ogren, J. A.: Determining Aerosol Radiative Properties Using the TSI 3563 Integrating Nephelometer, Aerosol Science and Technology, 29, 57–69, https://doi.org/10.1080/02786829808965551, 1998.

Ansmann, A., Petzold, A., Kandler, K., Tegen, I., Wendisch, M., Müller, D., Weinzierl, B., Müller, T., and Heintzenberg, J.: Saharan Mineral Dust Experiments SAMUM–1 and SAMUM–2: What Have We Learned?, Tellus B: Chemical and Physical Meteorology, 63, 403–429, https://doi.org/10.1111/j.1600-0889.2011.00555.x, 2011.

Bohren, C. F. and Huffman, D. R.: Absorption and scattering of light by small particles, John Wiley & Sons, https://doi.org/10.1002/9783527618156, 2008.

Bond, T. C., Anderson, T. L., and Campbell, D.: Calibration and Intercomparison of Filter-Based Measurements of Visible Light Absorption by Aerosols, Aerosol Science and Technology, 30, 582–600, https://doi.org/10.1080/027868299304435, 1999.

Bond, T. C., Covert, D. S., and Müller, T.: Truncation and Angular-Scattering Corrections for Absorbing Aerosol in the TSI 3563 Nephelometer, Aerosol Science and Technology, 43, 866–871, https://doi.org/10.1080/02786820902998373, 2009.

Davies, N. W., Fox, C., Szpek, K., Cotterell, M. I., Taylor, J. W., Allan, J. D., Williams, P. I., Trembath, J., Haywood, J. M., and Langridge, J. M.: Evaluating Biases in Filter-Based Aerosol Absorption Measurements Using Photoacoustic Spectroscopy, Atmospheric Measurement Techniques, 12, 3417–3434, https://doi.org/10.5194/amt-12-3417-2019, 2019.

Devon, M. J. and Rudin, A.: A Simple Technique for Measuring the Refractive Index of Polymer Latexes at Various Wavelengths, Journal of Applied Polymer Science, 34, 469–476, https://doi.org/10.1002/app.1987.070340202, 1987.

Gasteiger, J. and Wiegner, M.: MOPSMAP v1.0: A Versatile Tool for the Modeling of Aerosol Optical Properties, Geoscientific Model Development, 11, 2739–2762, https://doi.org/10.5194/gmd-11-2739-2018, 2018.

Gasteiger, J., Wiegner, M., GROß, S., Freudenthaler, V., Toledano, C., Tesche, M., and Kandler, K.: Modelling Lidar-Relevant Optical Properties of Complex Mineral Dust Aerosols, Tellus B, 63, 725–741, https://doi.org/10.1111/j.1600-0889.2011.00559.x, 2011.

Horvath, H.: Extrapolation of a Truncated Aerosol Volume Scattering Function to the Far Forward and Back Region, Journal of Aerosol Science, 90, 26–35, https://doi.org/10.1016/j.jaerosci.2015.08.001, 2015.

Horvath, H., Alados Arboledas, L., and Olmo Reyes, F. J.: Angular Scattering of the Sahara Dust Aerosol, Atmospheric Chemistry and Physics, 18, 17 735–17 744, https://doi.org/10.5194/acp-18-17735-2018, 2018.

Massoli, P., Murphy, D. M., Lack, D. A., Baynard, T., Brock, C. A., and Lovejoy, E. R.: Uncertainty in Light Scattering Measurements by TSI Nephelometer: Results from Laboratory Studies and Implications for Ambient Measurements, Aerosol Science and Technology, 43, 1064–1074, https://doi.org/10.1080/02786820903156542, 2009.

Mishchenko, M. I. and Mackowski, D. W.: Light Scattering by Randomly Oriented Bispheres, Optics Letters, 19, 1604–1606, https://doi.org/10.1364/OL.19.001604, 1994.

Müller, T., Laborde, M., Kassell, G., and Wiedensohler, A.: Design and Performance of a Three-Wavelength LED-based Total Scatter and Backscatter Integrating Nephelometer, Atmospheric Measurement Techniques, 4, 1291–1303, https://doi.org/10.5194/amt-4-1291-2011, 2011a.

Müller, T., Schladitz, A., Kandler, K., and Wiedensohler, A.: Spectral Particle Absorption Coefficients, Single Scattering Albedos and Imaginary Parts of Refractive Indices from Ground Based in Situ Measurements at Cape Verde Island during SAMUM-2, Tellus B: Chemical and Physical Meteorology, 63, 573–588, https://doi.org/10.1111/j.1600-0889.2011.00572.x, 2011b.

Müller, T., Virkkula, A., and Ogren, J. A.: Constrained Two-Stream Algorithm for Calculating Aerosol Light Absorption Coefficient from the Particle Soot Absorption Photometer, Atmospheric Measurement Techniques, 7, 4049–4070, https://doi.org/10.5194/amt-7-4049-2014, 2014.

Ogren, J. A.: Comment on "Calibration and Intercomparison of Filter-Based Measurements of Visible Light Absorption by Aerosols", Aerosol Science and Technology, 44, 589–591, https://doi.org/10.1080/02786826.2010.482111, 2010.

Ogren, J. A., Wendell, J., Andrews, E., and Sheridan, P. J.: Continuous Light Absorption Photometer for Long-Term Studies, Atmospheric Measurement Techniques, 10, 4805–4818, https://doi.org/10.5194/amt-10-4805-2017, 2017.

Onasch, T. B., Massoli, P., Kebabian, P. L., Hills, F. B., Bacon, F. W., and Freedman, A.: Single Scattering Albedo Monitor for Airborne Particulates, Aerosol Science and Technology, 49, 267–279, https://doi.org/10.1080/02786826.2015.1022248, 2015.

Petzold, A., Veira, A., Mund, S., Esselborn, M., Kiemle, C., Weinzierl, B., Hamburger, T., Ehret, G., Lieke, K., and Kandler, K.: Mixing of Mineral Dust with Urban Pollution Aerosol over Dakar (Senegal): Impact on Dust Physico-Chemical and Radiative Properties, Tellus B: Chemical and Physical Meteorology, 63, 619–634, https://doi.org/10.1111/j.1600-0889.2011.00547.x, 2011.

Petzold, A., Onasch, T., Kebabian, P., and Freedman, A.: Intercomparison of a Cavity Attenuated Phase Shift-based Extinction Monitor (CAPS PMex) with an Integrating Nephelometer and a Filter-Based Absorption Monitor, Atmospheric Measurement Techniques, 6, 1141–1151, https://doi.org/10.5194/amt-6-1141-2013, 2013.

Pfeifer, S.: Verknüpfung aerodynamischer und optischer Eigenschaften nichtkugelförmiger atmosphärischer Grobstaubpartikel, Ph.D. thesis, 2014.

Prahl, S.: Miepython, a pure Python module to calculate light scattering by non-absorbing, partially-absorbing, or perfectly conducting spheres. Mie theory is used, following the procedure described by Wiscombe., GitHub[code], https://miepython.readthedocs.io (last access:09.06.2020).

Schladitz, A., MüLLER, T., Kaaden, N., Massling, A., Kandler, K., Ebert, M., Weinbruch, S., Deutscher, C., and Wiedensohler, A.: In Situ Measurements of Optical Properties at Tinfou (Morocco) during the Saharan Mineral Dust Experiment SAMUM 2006, Tellus B: Chemical and Physical Meteorology, 61, 64–78, https://doi.org/10.1111/j.1600-0889.2008.00397.x, 2009.

Virkkula, A.: Correction of the Calibration of the 3-Wavelength Particle Soot Absorption Photometer ($3\lambda$ PSAP), Aerosol Science and Technology, 44, 706–712, https://doi.org/10.1080/02786826.2010.482110, 2010.

Virkkula, A., Ahlquist, N. C., Covert, D. S., Arnott, W. P., Sheridan, P. J., Quinn, P. K., and Coffman, D. J.: Modification, Calibration and a Field Test of an Instrument for Measuring Light Absorption by Particles, Aerosol Science and Technology, 39, 68–83, https://doi.org/10.1080/027868290901963, 2005.

von der Weiden, S.-L., Drewnick, F., and Borrmann, S.: Particle Loss Calculator – a New Software Tool for the Assessment of the Performance of Aerosol Inlet Systems, Atmospheric Measurement Techniques, 2, 479–494, https://doi.org/10.5194/amt-2-479-2009, 2009.

Wiscombe, W. J.: Improved Mie Scattering Algorithms, Applied Optics, 19, 1505–1509, https://doi.org/10.1364/AO.19.001505, 1980.

Yurkin, M. A. and Hoekstra, A. G.: The Discrete-Dipole-Approximation Code ADDA: Capabilities and Known Limitations, Journal of Quantitative Spectroscopy and Radiative Transfer, 112, 2234–2247, https://doi.org/10.1016/j.jqsrt.2011.01.031, 2011.